



Technical Note

Novel Airborne EM Image Appraisal Tool for Imperfect Forward Modeling

Wouter Deleersnyder^{1,2,*} , David Dudal^{2,3} and Thomas Hermans¹

¹ Laboratory of Applied Geology and Hydrogeology, Department of Geology, Ghent University, Krijgslaan 281-S8, 9000 Ghent, Belgium

² Department of Physics, KU Leuven Campus Kortrijk—KULAK, Etienne Sabbelaan 53, 8500 Kortrijk, Belgium

³ Department of Physics and Astronomy, Ghent University, Ghent, Krijgslaan 281-S9, 9000 Ghent, Belgium

* Correspondence: wouter.deleersnyder@kuleuven.be

Abstract: Full 3D inversion of time-domain Airborne ElectroMagnetic (AEM) data requires specialists' expertise and a tremendous amount of computational resources, not readily available to everyone. Consequently, quasi-2D/3D inversion methods are prevailing, using a much faster but approximate (1D) forward model. We propose an appraisal tool that indicates zones in the inversion model that are not in agreement with the multidimensional data and therefore, should not be interpreted quantitatively. The image appraisal relies on multidimensional forward modeling to compute a so-called normalized gradient. Large values in that gradient indicate model parameters that do not fit the true multidimensionality of the observed data well and should not be interpreted quantitatively. An alternative approach is proposed to account for imperfect forward modeling, such that the appraisal tool is computationally inexpensive. The method is demonstrated on an AEM survey in a salinization context, revealing possible problematic zones in the estimated fresh–saltwater interface.

Keywords: airborne geophysics; AEM; TEM; resistivity; conductivity; appraisal; modeling; electromagnetics



Citation: Deleersnyder, W.; Dudal, D.; Hermans, T. Novel Airborne EM Image Appraisal Tool for Imperfect Forward Modeling. *Remote Sens.* **2022**, *14*, 5757. <https://doi.org/10.3390/rs14225757>

Academic Editors: Gerardo Di Martino and Antonio Iodice

Received: 8 September 2022

Accepted: 11 November 2022

Published: 14 November 2022

Publisher's Note: MDPI stays neutral with regard to jurisdictional claims in published maps and institutional affiliations.



Copyright: © 2022 by the authors. Licensee MDPI, Basel, Switzerland. This article is an open access article distributed under the terms and conditions of the Creative Commons Attribution (CC BY) license (<https://creativecommons.org/licenses/by/4.0/>).

1. Introduction

The Airborne ElectroMagnetic induction (AEM) method is a practical tool to map near-surface geological features over large areas, as electromagnetic induction methods are sensitive to the bulk resistivity. It is increasingly used for mineral exploration [1], hydrogeological mapping [2,3], saltwater intrusion [4–6] and contamination [7]. AEM methods will become more and more important for the challenges in the future, e.g., as an important investigation method for groundwater management. It is the only viable approach to providing hydrogeological mappings on a large scale. Among the geophysical EM methods, the advancement of the AEM within the last two decades was eminent. While the AEM systems have massively advanced [8], the data interpretation process and the related computational burden remains a main impediment. Full 3D inversion is an active research area [9–15]. It requires specialists' expertise and a tremendous amount of computational resources, not readily available to everyone. Consequently, quasi-2D and quasi-3D inversion methods are prevailing, using a much faster but approximate (1D) forward model. While using a 1D forward model is valid for slowly varying lateral variations, the hypothesis is not always valid. The question remains whether the obtained inversion results are reliable and can be interpreted quantitatively. In this work, we do not want to dissuade the use of 1D forward models for AEM interpretation. Rather, we argue that an additional step after each inversion with an approximate forward model should be added using an image appraisal tool, to verify that no erroneous interpretation has occurred as a result of the approximate forward model. The tool indicates uncertain areas in the recovered model, which should be interpreted with extra care or should be

reinterpreted using a full 3D inversion. In the latter case, this computationally demanding 3D inversion must, fortunately, only be performed on a subset of the original dataset.

Appraisal tools usually address resolution issues. They are commonly used in electrical resistivity tomography [16–18], with e.g., Paepen et al. [19] showing an application directly functional in a saltwater intrusion context. Specifically for EM, Alumbaugh and Newman [20] provide an appraisal tool based on the resolution matrix, which provides insight on the resolution and accuracy of the recovered images. Christiansen and Christensen [21] provide a quantitative appraisal for AEM by adding a comparison to ground-based data. The method relies on 1D forward modeling and does not account for multidimensionality effects.

To overcome the latter shortcomings, we propose a novel appraisal tool that can detect wrongly fitting multidimensional data, i.e., zones in the inversion model that are not in agreement with the multidimensional (2D/3D) forward model and, therefore, should not be interpreted in a quantitative fashion. To our knowledge, such a tool has never been presented in the scientific literature. As generating multidimensional data in a time-domain AEM setting can be challenging, a successful, alternative approach is presented to function with imperfect forward 2/3D modeling. This allows for more accessible, computationally tractable computations on coarser discretizations on a single laptop with only a fraction of the required resources for perfect modeling.

2. Method

2.1. Three Types of Forward Modeling

The forward model describes the subsurface's response to a specific subsurface realization and a specific survey set-up. There are two main common approaches: The first is based on (semi-)analytical models that solve the (continuous) Maxwell equations for a one-dimensional subsurface model, meaning that it assumes horizontal layers without lateral variations. An open-source Python implementation by Werthmüller [22] neatly implements such a forward model by Hunziker et al. [23] in a fast and reliable fashion. We refer to this model as the low-fidelity model (LF), as it cannot account for lateral variations in the subsurface model. The second approach is based on a discretization of the physics on a mesh. Those simulations mimic the full 3D soil response of the potentially non-1D subsurface and allow for multidimensional modeling. In this work, the finite volume method from the open-source package SimPEG [10] is used. With a suitable discretization of the geometry, an accurate magnetic field response can be obtained. In the case of perfect forward modeling, we refer to these simulations as the high-fidelity model (HF). However, numerical simulations are not always accurate, and the term high-fidelity should be used with caution. If the accuracy of the simulations is limited due to the computational burden requiring the use of a coarse mesh, the response contains a modeling error. That modeling error is different in origin than the one introduced by only considering a one-dimensional subsurface and depends on the discretization of the user and subsurface model. We refer to this model as the medium-fidelity model (MF). We visualized the various types of modeling in Figure 1.

2.2. Quasi-2D Inversion

In most geophysical inverse problems, the inversion model \mathbf{m} consists of electrical conductivities (EC) and fits the observed data \mathbf{d}^{obs} and is simple in Occam's sense [24]. This is accomplished by minimizing an objective function:

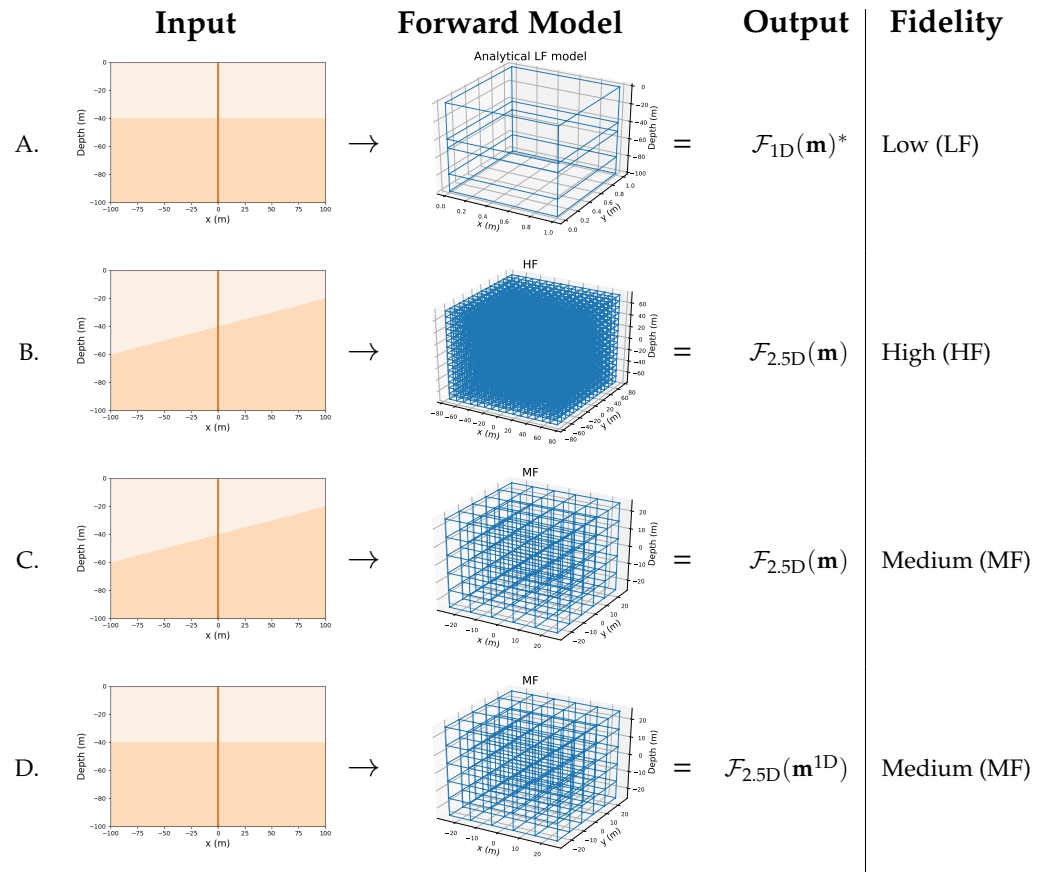
$$\phi(\mathbf{m}) = \phi_d(\mathbf{m}) + \beta\phi_m(\mathbf{m}), \quad (1)$$

where ϕ_d and ϕ_m are, respectively, the data and model misfit. β is a regularization parameter that balances the relative importance of the two misfits.

In quasi-2D inversion, the data misfit:

$$\phi_d(\mathbf{m}) = \frac{1}{n} \left\| \mathbf{W}_d \left(\mathbf{d}^{\text{obs}} - \mathcal{F}_{1D}(\mathbf{m}) \right) \right\|_2^2 \quad (2)$$

uses a 1D approximation for the forward (LF) model $\mathcal{F}_{1D}(\mathbf{m})$, which significantly reduces the computation time of the inversion procedure. The model misfit ϕ_m promotes smooth solutions [24,25].



* In the 1D case, notation $\mathcal{F}_{1D}(\mathbf{m}) = \mathcal{F}_{1D}(\mathbf{m}^{1D})$.

Figure 1. Conceptual visualization of the various forward data types used. The input is either a multidimensional subsurface model (B,C) or a 1D subsurface model (in a moving footprint approach) (A,D). The forward model is either a Low-Fidelity (LF) analytical forward model (with depths and EC as input) (see A), a High-Fidelity (HF) forward simulation on an accurate mesh (B) or a Medium-Fidelity (MF) forward simulation on an inaccurate (coarser) mesh (C,D). NOTE: the presented meshes are illustrative and are not the ones used for multidimensional modeling. Some details on the MF and HF mesh are described in Appendix A.

In this work, the regularization parameter β is selected via the chi-squared criterion, meaning that an optimal inversion model fits the observed data to a noise-weighted RMS. The diagonal matrix \mathbf{W}_d contains the noise-levels, that is the reciprocals of the estimated noise standard deviation and the noise floor. The latter ensures that not too much weight is given to the last channels, as they are highly sensitive to measurement error due to their small absolute value (in this work, the noise floor is set to 10^{-13}). As we work with two forward models, we distinguish two RMS errors:

$$\epsilon_{1D} = \sqrt{\frac{1}{n} \|\mathbf{W}_d(\mathbf{d}^{\text{obs}} - \mathcal{F}_{1D}(\mathbf{m}))\|_2^2}, \quad \epsilon_{2.5D} = \sqrt{\frac{1}{n} \|\mathbf{W}_d(\mathbf{d}^{\text{obs}} - \mathcal{F}_{2.5D}(\mathbf{m}))\|_2^2}, \quad (3)$$

where $\mathcal{F}_{2.5D}$ refers to either the high- or medium-fidelity forward model, which better allow for 2D variations on a 3D mesh. The approach could be extended without loss of generality to a full 3D forward model, meaning that 3D variations are modeled on a 3D mesh.

2.3. Normalized Gradient

The multidimensional sensitivity matrix or Jacobian $\mathbf{J} \left(= \frac{\partial \mathbf{d}}{\partial \mathbf{m}} \right)$ is required to map poorly fitting data points to specific areas of the inversion model. A high sensitivity value signifies that a change of this parameter influences the predicted data strongly. We propose to compute the sensitivity matrix \mathbf{J}_i on a coarse 3D mesh with a strongly reduced mesh size and number of cells, optimized for computing the response for one sounding and allowing for a computation on a single laptop/desktop. This strategy combines the moving footprint approach [15] and that of Zhang et al. [26].

With the computed data, the normalized gradient $\tilde{\nabla} \phi_{d,2.5D}$ is computed as follows:

$$\tilde{\nabla} \phi_{d,2.5D} = \frac{\sum_i |\mathbf{J}_i^T \mathbf{W}_d (\mathbf{d}_i^{\text{obs}} - \mathcal{F}_{2.5D}(\mathbf{m})_i)|}{\sum_i |\mathbf{J}_i^T|}, \quad (4)$$

where i refers to a specific sounding. Note that this computation may involve an interpolation step to map all data to, for example, the discretization of the recovered model. We are mainly interested in the relative importance of each zone in the inversion model, hence the denominator. The normalized gradient $\tilde{\nabla} \phi_{d,2.5D}$ gives an indication for which model parameters would change in a full 2D inversion, meaning that those model parameters do not fit the data well with a multidimensional forward model. Put differently, model parameters that would not rapidly change are likely to be fitting the data well and can be interpreted quantitatively.

2.4. Accounting for Imperfect Modeling

The image appraisal method does not need to be used with an expensive, exact high-fidelity forward model $\mathcal{F}_{2.5D}$. If a medium-fidelity model is used, the predicted data $\mathcal{F}_{2.5D}(\mathbf{m})$ for the recovered model will not fit the observed data \mathbf{d}^{obs} as well as the 1D forward model \mathcal{F}_{1D} , which we refer to as the forced modeling error approach. However, our method will still identify in which zone of the model multi-dimensional effects are significant.

In this approach, the model parameters right below the sounding location are fed as a 1D subsurface model to the imperfect 2.5D medium-fidelity forward model $\mathcal{F}_{2.5D}$. As a result, we obtain less accurate data than with the 1D forward model \mathcal{F}_{1D} , but with similar modeling errors per gate time. The normalized gradient (4) is otherwise identical, but \mathbf{d}^{obs} is replaced by $\mathcal{F}_{2.5D}(\mathbf{m}^{1D})$, where \mathbf{m}^{1D} represents the 1D subsurface model per sounding, which is generated from the recovered model. This approach is demonstrated in Section 3.1.2.

3. Results

In this section, we apply our proposed methodology on a synthetic model and a real field data case within a saltwater intrusion context [27], both with the time-domain AEM data from a dual moment (LM+HM) SkyTEM instrument [28].

3.1. Synthetic Model

Any appraisal method for multidimensional effects should indicate areas in the recovered model that potentially do not fit the true multidimensionality of the observed data well. Simultaneously, it should not indicate areas in the recovered model where there appear to be no issues with data interpretation. For field data, where the true subsurface parameters are unknown, our proposed method is difficult to validate. Therefore, a simple subsurface model was created to demonstrate and verify the performance of our method, before applying it to real field data in Section 3.2.

Consider the recovered model in Figure 2B, which consists of two layers of 0.05 S/m and 0.5 S/m, respectively. The model is selected based on the discrepancy principle (Figure 2A), which states that the optimal value for the regularization parameter corresponds to the case in which the data fits up to the noise level, i.e., $\phi_d \approx 1$ [29]. The recovered model has a noise-weighted error ϵ_{1D} of 1.02, while with the multidimensional data $\epsilon_{2.5D}$ is 1.53. The latter indicates that the model does not fit the data to its noise level when an HF, multi-dimensional forward model is used. The predicted data with the low-fidelity model and the observed data points are presented in Figure 2C,D, where the slight discrepancy in the late HM time channels are ascribed to the noise floor. In the recovered model, the interface between both layers changes abruptly at $x = 700$. Near the interface, the recovered model suggests a dipping layer and the interpretation can be erroneous without taking into account the use of the 1D forward model for the generation of the recovered model.

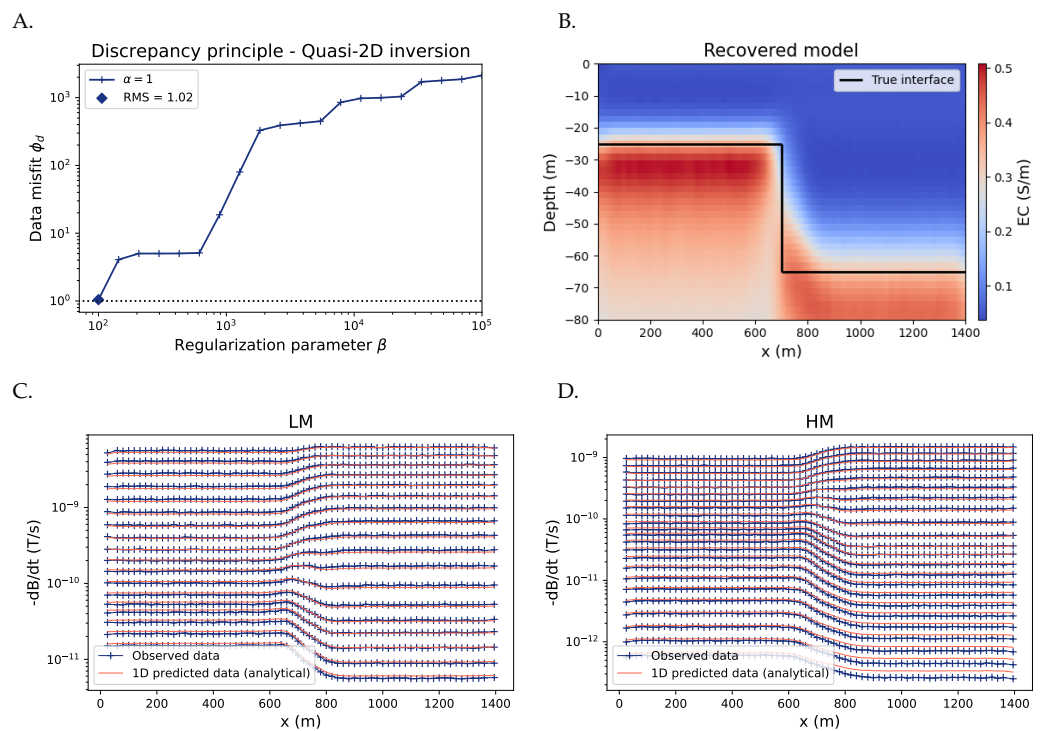


Figure 2. Quasi-2D inversion results. (A) Discrepancy principle for the selection of the optimal regularization parameter β . (B) Recovered model. (C,D) Observed and predicted data (time-domain electromagnetic induction data) with a 1D analytical forward model \mathcal{F}_{1D} .

3.1.1. Perfect Modeling Approach

The first approach compares the predicted multidimensional data ($\mathcal{F}_{2.5D}$) with the observed data \mathbf{d}^{obs} . In Figure 3A,B, the green dashed line from the predicted data $\mathcal{F}_{2.5D}(\mathbf{m})$ clearly deviates between 600 m and 800 m from the observed data points. The individual noise-weighted errors are also shown in Figure 3C. For some soundings between $n^\circ 30$ and $n^\circ 40$ in Figure 3C, where $\mathbf{d}^{\text{obs}} = \mathcal{F}_{2.5D}(\mathbf{m})$, the inversion model *appears* to fit the multidimensional data, which is an anticipated behavior with this kind of subsurface model that cannot be determined objectively in a general fashion (for an unknown subsurface model). As the sensitivity functions overlap with neighboring soundings, this poses no problems and this alleged perfect fit will also come into the scope of the appraisal method, which is evidently a plus.

The normalized gradient is shown in Figure 3D, which must be considered together with the recovered model. The larger (darker) the normalized gradient, the more likely the interpretation in the area is incorrect. In Figure 3E,F, the recovered model is shown where cells are left white if they are larger than a certain cut-off value, set by the user. In our case, that is if they are larger than 20% or 50% of the maximum value in the normalized gradient (conservative, resp. optimistic case). The user can, as it were, scroll from a max normalized gradient to smaller values to get an indication of which areas are more/less likely to be correct.

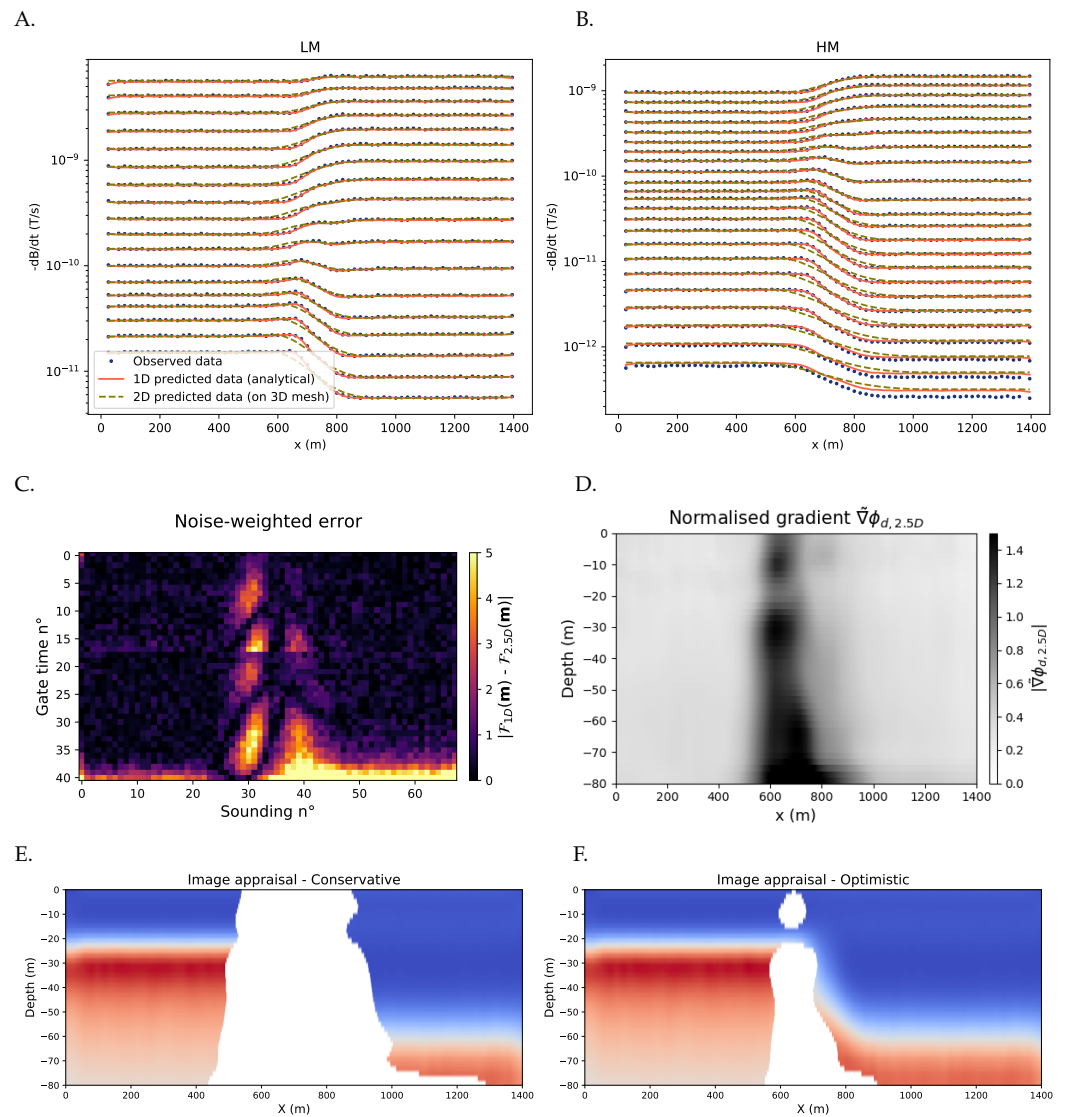


Figure 3. Image appraisal with *perfect* forward modeling. (A,B) A discrepancy mainly near the $x = 700$ m interface. (C) The individual noise-weighted errors. The first 18 gate times correspond to the LM and the 23 last gate times to the HM. (D) The normalized gradient indicates areas near the $x = 700$ m interface. (E,F) Image appraisal outcomes clearly indicate problematic areas in the region near the ‘step’.

3.1.2. Imperfect Modeling—Approach with Forced Modeling Error

The second approach uses a medium-fidelity model to compute the 1D model response. The model parameters right below the sounding location are used, as in the quasi-2D inversion scheme, and extended/projected to construct horizontally stratified layers to be used in the simulation. When using the same 2.5D forward model on the 1D model, a similar modeling error is expected to the 2.5D data (while of course, we have used a faster and

more accurate 1D forward model \mathcal{F}_{1D} throughout the inversion). Then, the obtained data $\mathcal{F}_{2.5D}(\mathbf{m}^{1D})$ can be compared to $\mathcal{F}_{2.5D}(\mathbf{m})$ to get an idea of where the multidimensionality of the observed data is not well fitted. In Equation (4), \mathbf{d}^{obs} is replaced with $\mathcal{F}_{2.5D}(\mathbf{m}^{1D})$. A disadvantage of this method is that the observed data is no longer used. The advantage is that it is not required to work with (robust) selection methods to eliminate the modeling error (which can potentially fail for poorly designed meshes).

The procedure behind the image appraisal is analogous to the previous approach in Section 3.1.1. Contrary to the previous method, additional data is generated with the 2.5D forward model $\mathcal{F}_{2.5D}$ of the 1D version of the recovered version $\mathcal{F}_{2.5D}(\mathbf{m}^{1D})$. This data is presented in Figure 4A,B as the green dashed line. It is apparent that the predicted data $\mathcal{F}_{2.5D}(\mathbf{m}^{1D})$ and $\mathcal{F}_{2.5D}(\mathbf{m})$ overlap at the horizontal parts of the recovered model, while a deviation is observed at the transition near $x = 700$ m. The predicted seems to follow the trend in the observed data well, while the exact value is quite different. This should be ascribed to the multidimensionality of the step at $x = 700$ m, but the imperfect modeling of the MF forward model. More background is provided in Appendix A and in Figure A1, more specifically. The noise-weighted errors are no less than $\epsilon_{1D} = 14.6$ and $\epsilon_{2.5D} = 14.7$, signalling a significant modeling error. The absolute values of the noise-weighted errors with respect to the true observed data are shown in Figure 4C. The errors around $x = 700$ m are prominent. The normalized gradient is presented in Figure 4B; it closely resembles the normalized gradient with perfect modeling. The image is less noisy, as we are no longer comparing with the observed data, and thus, the measurement error is lacking. The resulting image appraisal images are presented in Figure 4C,D, and are very similar to the results from Section 3.1.1, thereby reconfirming the interpretation made there.

To illustrate the reduction in the computational burden, for the data production for a single sounding on the precise mesh for perfect modeling in Section 3.1.1, 1 h and 20 min of computation time were required on 36 cores of an HPC infrastructure node (2×18 -core Intel Xeon Gold 6140 (Skylake @ 2.3 GHz)) and required 150 GB of RAM. The simulations on the coarse mesh for imperfect modeling were performed in just a few seconds on a laptop with Apple's M1 chip and 10 cores and with negligible memory usage.

3.2. Field Data Case

The image appraisal method is applied on time-domain AEM data with the setup described in Delsman et al. [27]. The inversion model in Figure 5 is obtained via quasi-2D inversion. The obtained inversion model has ϵ_{1D} of 0.97, while 2.9 for $\epsilon_{2.5D}$. The result shows low values of Electrical Conductivity (EC) at shallow depths and high values of EC between 20 m and 50 m depth, which corresponds to a saltwater lens resting on a clay layer. There is quite some lateral variation, so this is an interesting case for our appraisal tool.

The normalized gradient $\tilde{\nabla} \phi_{d,2.5D}$ for both approaches is shown in Figures 6 and 7. In this case, one can see the effect of working with the observed data \mathbf{d}^{obs} and the medium fidelity data $\mathcal{F}_{2.5D}(\mathbf{m}^{1D})$ well. The recovered model in Figure 5 generally fits the late gate times less well (the broad layer around gate time $n^\circ 30$ in Figure 6A), creating a relatively present dark layer in the normalized gradient from a depth of 30 m onwards, not necessarily due to multidimensionality issues. The perfect modeling (Figure 6) gives a more general picture of which areas of the recovered model do not fit the observed data well, whatever the reason (multidimensionality, misfit related to noise). The optimistic image appraisal in Figure 6D shows that especially the fresh–saltwater interface around 600–800 m should not be interpreted quantitatively. This is also the conclusion from the image appraisal with imperfect modeling in Figure 7D. Here, the observed data is no longer used and one only gets a picture of areas that do not fit the multidimensionality well (the band around gate time $n^\circ 30$ is missing in Figure 7A, while poorly fitting data points are now focused near specific soundings). Our image appraisal analysis teaches one that multidimensional inversion would be advised in the part from 400 to 800 m.

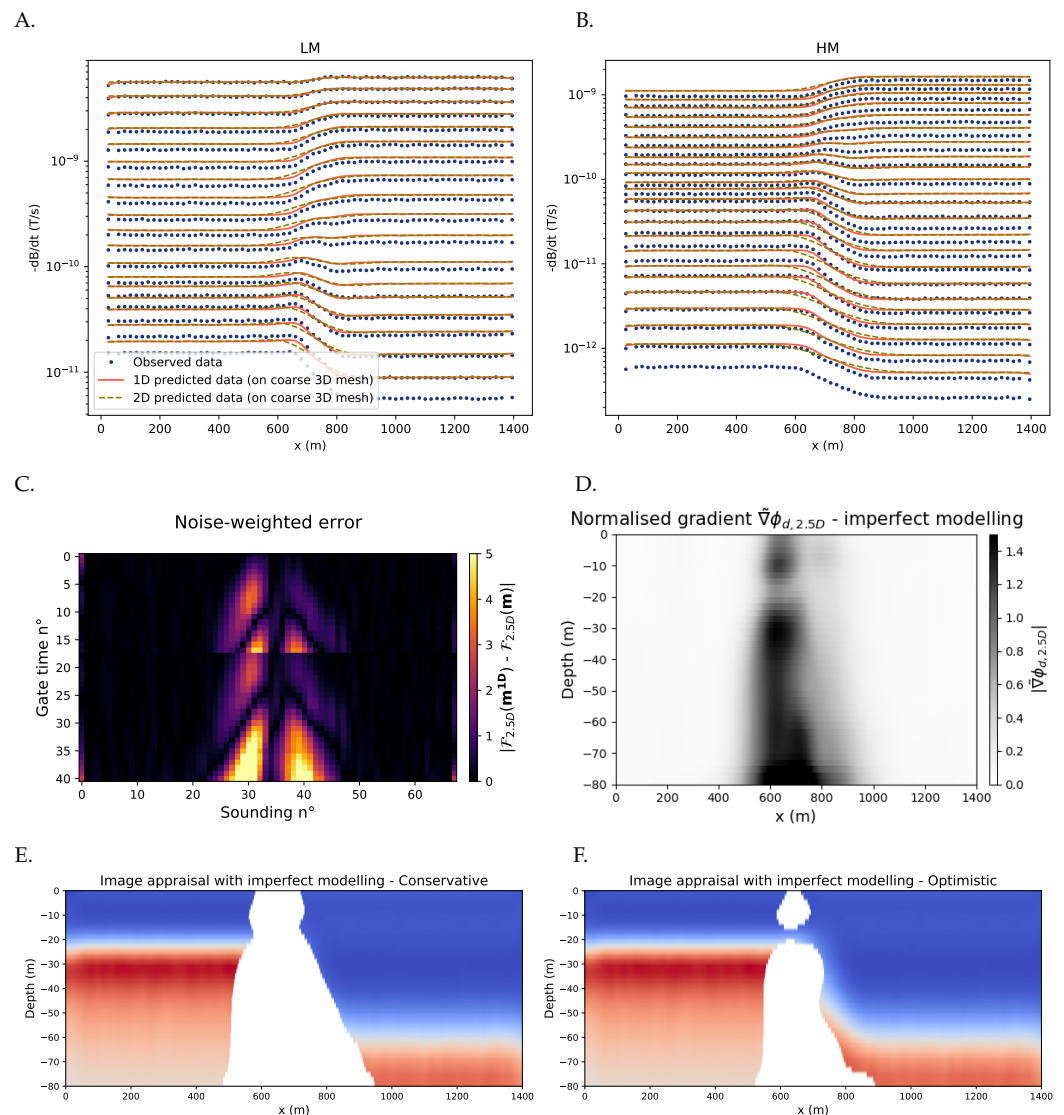


Figure 4. Image appraisal with *imperfect* forward modeling approach. (A,B) A discrepancy mainly near the $x = 700$ m interface. (C) The individual noise-weighted errors. The first 18 gate times correspond to the LM and the 23 last gate times to the HM. (D) The normalized gradient indicates areas near the $x = 700$ m interface. (E,F) Image appraisal outcomes clearly indicate problematic areas in the region near the ‘step’.

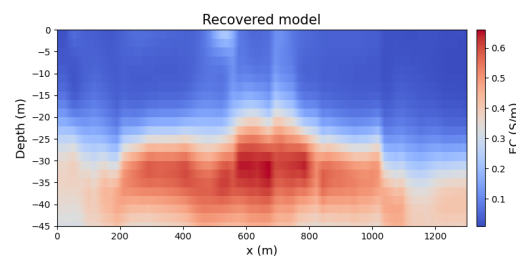


Figure 5. Recovered model from real field data from Delsman et al. [27].

Also note that the identified areas are not only zones with sharp conductivity variations. One could argue that the user who knows the 1D approximation would be careful to interpret in such zone, but the results illustrate that this is not sufficient. On the other hand, the tool does not tell if a 2D inversion would result in a significantly different 2D/3D inversion. It primarily indicates zones that might be sensitive to multidimensionality effects.

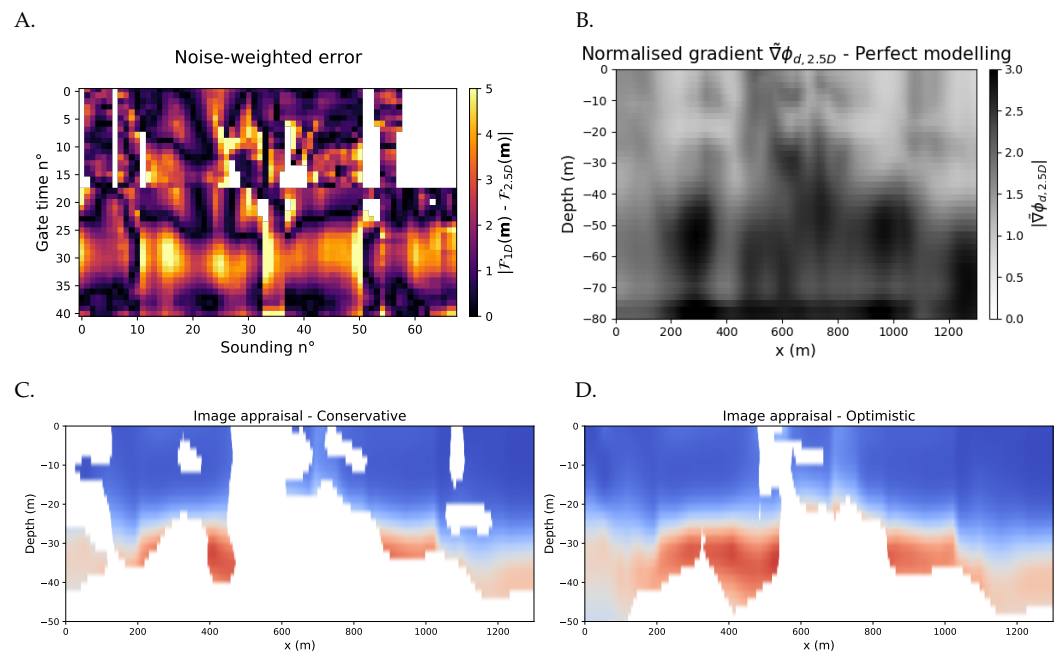


Figure 6. Image appraisal on real field data with *perfect* forward modeling approach. The individual noise-weighted errors in (A) include observed noise. The normalised gradient (B) for different cut-off values are shown in (C,D).

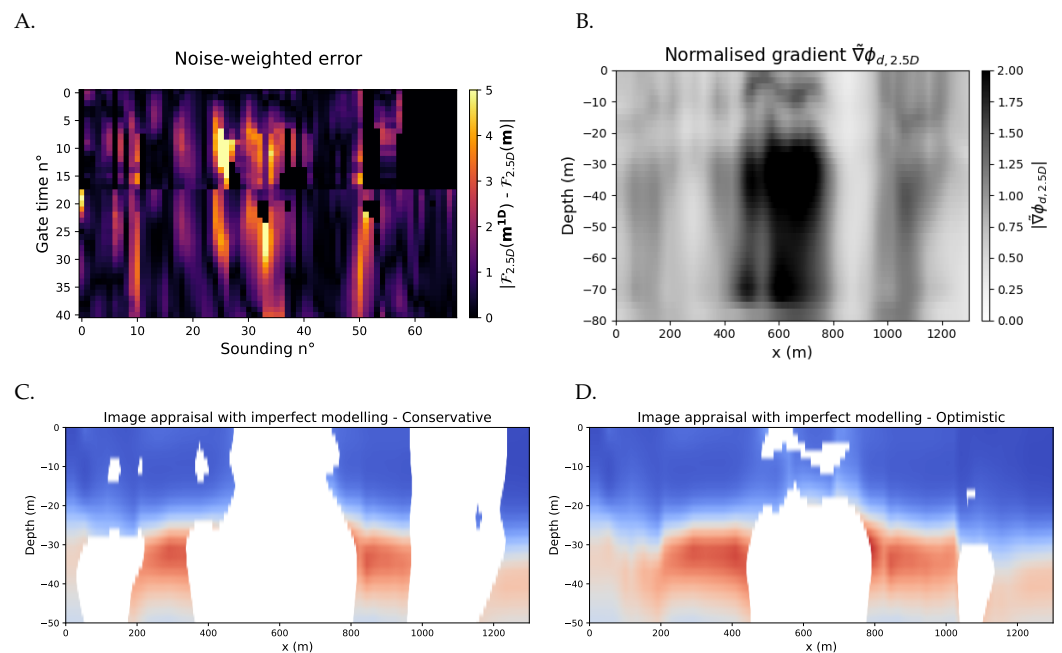


Figure 7. Image appraisal on real field data with *imperfect* forward modeling approach. The individual noise-weighted errors in (A) do not include observed noise. The normalised gradient (B) for different cut-off values are shown in (C,D).

4. Conclusions

We have proposed a computationally inexpensive image appraisal tool for AEM inversion. It enables assessment of an inversion model obtained with a low-fidelity (approximate) forward model for areas that are not fitting the true multidimensionality of the observed data, because it deviates from the 1D assumption. Adding this step to any quasi-2D or -3D method prevents one from quantitatively interpreting the problematic areas in the inversion model. If sufficient computational resources are available, the uncertain zones

in the recovered model can be reinterpreted with 3D inversion, instead of performing 3D inversion on the whole dataset. Furthermore, a forced modeling approach allows computationally less demanding simulations on an imperfect discretization to identify zones for which multidimensionality likely plays a role.

Thinking about general applications, cf. our method, the specific context of the reader's research will determine which of the two approaches is more desirable. If an HPC infrastructure is available, the perfect modeling will generate more general appraisal images (locating areas which are poorly fitting the observed data). When limited computational resources are available, the forced modeling error approach is more feasible (only requiring a fraction of the perfect modeling resources), focusing on multidimensionality issues only.

Author Contributions: Conceptualization, W.D.; methodology, W.D.; software, W.D.; validation, W.D.; writing—original draft preparation, W.D.; writing—review, T.H. and D.D.; supervision, D.D. and T.H.; funding acquisition, D.D. and T.H. All authors have read and agreed to the published version of the manuscript.

Funding: The research leading to these results has received funding from FWO (Fund for Scientific Research, Flanders, grant 1113020N and 1113022N) and the Flemish Institute for the Sea (VLIZ) Brilliant Marine Research Idea 2022. The resources and services used in this work were provided by the VSC (Flemish Supercomputer Center), funded by the Research Foundation - Flanders (FWO) and the Flemish Government.

Informed Consent Statement: Not applicable.

Data Availability Statement: The field data from Delsman et al. [27] used for the analysis in Section 3.2 are available at Zenodo [30] via <https://doi.org/10.5281/zenodo.7015419> (accessed on 1 May 2022) with CC-BY 4.0 license. Scripts that control the above software and produce the appraisal results [31] are available from Zenodo via <https://doi.org/10.5281/zenodo.7015876> (accessed on 1 May 2022) with the CC-BY 4.0 license and developed at https://github.com/WouterDls/AEM_appraisal (accessed on 1 May 2022)..

Acknowledgments: We thank VMM (Flanders Environment Agency) for making available the field data.

Conflicts of Interest: The authors declare no conflict of interest.

Appendix A. Practical Guide for Constructing a Medium/High-Fidelity Mesh

The multidimensional data are simulated via the finite volume method, a numerical discretization technique for representing and solving partial differential equations (here: Maxwell equations) in the form of algebraic equations. SimPEG [10,32] is used in this work, which is an open-source Python package for 3D simulations on a mesh (and other functionalities, such as inversion). As we rely on the moving footprint approach [15], we focus on a suitable mesh that we can use for each sounding (and thus no multiple sources and receivers on one larger mesh). A suitable mesh has smaller cell sizes in crucial areas where the physical quantities significantly vary, e.g., right below the surface. We are working on time-dependent problems, therefore, smaller time steps have to be considered when the physical quantities are changing rapidly. This, in turn, depends on the electrical conductivity (the more resistive, the faster the currents dissipate both downwards and laterally, similar to smoke rings). A good spatial and temporal discretization should be small at crucial stages of the underlying physics to ensure good accuracy, but should also balance the computational burden.

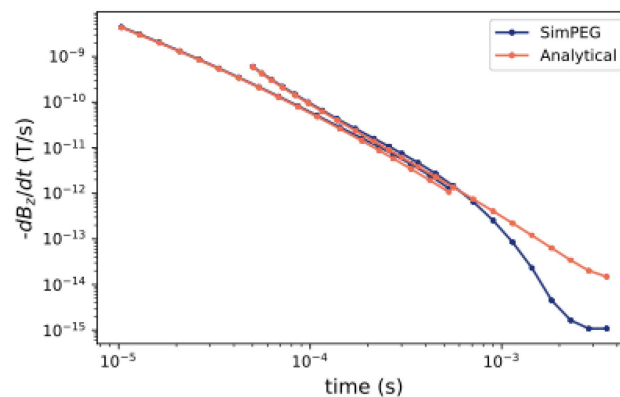


Figure A1. When comparing the generated data via simulation software with an exact forward model, one can get an indication of how to improve the mesh. In this case, where the late time channels break down, the mesh size should be increased.

To construct a mesh, we have used the following strategy: it is a rule of thumb that for time-domain problems, the appropriate cell sizes can be determined from the expected diffusion distance d [33], i.e.,

$$d = \sqrt{\frac{2t}{\mu\sigma}}, \quad (\text{A1})$$

where the relation with conductivity is apparent. Note that this expression only holds for homogeneous halfspaces. From this quantity, we determine that the smallest cell size should be no larger than 10% of the smallest diffusion distance and the thicknesses of the padding should be at least three times the maximum diffusion distance. Depending on the specifics of the survey set-up and the expected conductivities, the simulated data for a homogeneous halfspace can be compared to an exact semi-analytical forward model [23]. For example, for a 10 mS/m halfspace, we could get the result from Figure A1. From a first look, there is a good correspondence for the LM and the early times of the HM. Clearly, at later times, there is a discrepancy. We exploit our understanding of the underlying physics to resolve this issue. The breaking down at late times suggests that the physical dimensions of the mesh are too small (the far away dissipated currents ‘do not fit’ on the mesh). For resistive media, the currents dissipate more quickly and consequently, a larger mesh is required. For a homogeneous halfspace of 100 mS/m, the mesh would have been suitable.

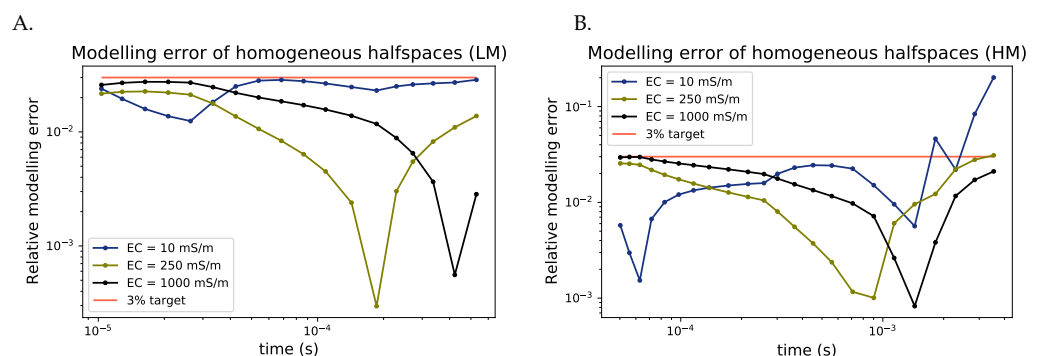


Figure A2. The relative modeling error of a homogeneous halfspace for the dual moment SkyTEM set-up, compared to the semi-analytical forward model for the Low Moment (A) and High Moment (B).

A discrepancy at early time gates indicates that the smallest cell sizes are too large. Furthermore, a smaller time stepping could solve the problem. It is a process of trial and error, balancing speed and accuracy.

For our work, we have set the target of the modeling error to max. 3%, a typical measurement noise level. This target has to hold for electrical conductivities ranging between 10 mS/m and 1000 mS/m. The relative modeling error per time channel is shown in Figure A2A,B. For the electrical conductivities of 10 mS/m, we abandon the target for later times in the HM, as we will never encounter such a low conductivity for the whole halfspace (the eddy currents will reach a higher conductive area faster than the late times channels, and for higher conductive halfspaces, the accuracy is higher). We also abandon the requirement for the last time channel for all conductivities, as we believe that the additional accuracy is not worth the additional extra computational cost. This is indeed not an issue, because the last time channel is typically close to the noise floor, for which the inverse problem already allows for a larger data misfit.

The above rationale was used to construct the high-fidelity mesh for this work. A suitable mesh thus depends on the context of the problem, where setting and loosening the targets should be carefully considered, as well as the computational burden. For the MF, the above requirements do not hold. The mesh is spatially too small (this can be clearly seen in Figure 4B, where the last time channel has a large discrepancy with the observed data) and the time-stepping is not optimized. The main requirement is always the computational practicality.

For constructing the MF mesh, we suggest to start from an HF mesh. For example, by doubling the smallest cell size of the HF mesh and halving the mesh size. For the time stepping, one allows larger time steps at earlier times. One keeps adjusting those parameters until the computation time is acceptable, the user again decides on the balance between computational burden and accuracy. The generated data and gradient will be highly inaccurate, but this poses no problems for the identification of multidimensionality issues: the generated data are solely compared with other data from this MF mesh (with similar modeling errors) and the gradient will still indicate the relevant area in the inversion mesh leading to the specific data (see, e.g., Zhang et al. [26]).

In this work, we reduced the HF mesh from Figure A3A with 1,284,795 cells to an MF mesh with 12,760 cells in Figure A3B. The smallest cell size is 0.05-by-0.5 and 4-by-10 for the HF and MF mesh, respectively. The spatial dimensions are also reduced: the furthest point on the HF mesh is at 1500 m from the origin, while it is at 675 in the MF mesh. In the HF mesh, 700 time steps are considered, while only 90 time steps are considered in the MF mesh. The specific details of both meshes can be found in Deleersnyder [31] and Deleersnyder et al. [34].

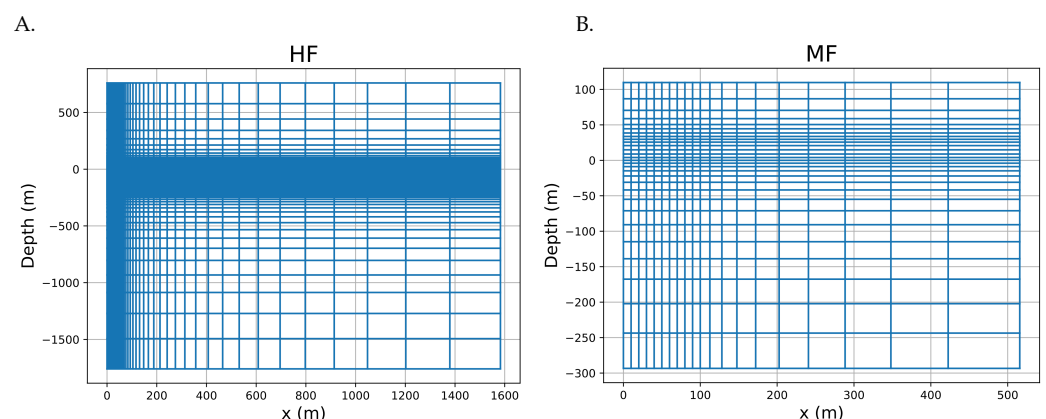


Figure A3. Cross-section of the 3D meshes used in this work, indicating regions with higher cell densities. (A) High-Fidelity (HF) mesh with 1,284,795 cells. (B) Medium-Fidelity (MF) mesh with 12,760 cells.

References

- Macnae, J.; Milkereit, B. Developments in broadband airborne electromagnetics in the past decade. *Proc. Explor.* **2007**, *7*, 387–398.
- Mikucki, J.A.; Auken, E.; Tulaczyk, S.; Virginia, R.; Schamper, C.; Sørensen, K.; Doran, P.; Dugan, H.; Foley, N. Deep groundwater and potential subsurface habitats beneath an Antarctic dry valley. *Nat. Commun.* **2015**, *6*, 1–9. [[CrossRef](#)] [[PubMed](#)]
- Podgorski, J.E.; Auken, E.; Schamper, C.; Vest Christiansen, A.; Kalscheuer, T.; Green, A.G. Processing and inversion of commercial helicopter time-domain electromagnetic data for environmental assessments and geologic and hydrologic mapping. *Geophysics* **2013**, *78*, E149–E159. [[CrossRef](#)]
- Goebel, M.; Knight, R.; Halkjær, M. Mapping saltwater intrusion with an airborne electromagnetic method in the offshore coastal environment, Monterey Bay, California. *J. Hydrol. Reg. Stud.* **2019**, *23*, 100602. [[CrossRef](#)]
- Siemon, B.; van Baaren, E.; Dabekaussen, W.; Delsman, J.; Dubelaar, W.; Karaoulis, M.; Steuer, A. Automatic identification of fresh–saline groundwater interfaces from airborne electromagnetic data in Zeeland, the Netherlands. *Surf. Geophys.* **2019**, *17*, 3–25.
- Deleersnyder, W.; Maveau, B.; Hermans, T.; Dudal, D. Flexible quasi-2D inversion of time-domain AEM data, using a wavelet-based complexity measure. *arXiv* **2022**, arXiv:2205.06458.
- Pfaffhuber, A.A.; Lysdahl, A.O.; Sørmo, E.; Skurdal, G.H.; Thomassen, T.; Anschütz, H.; Scheibz, J. Delineating hazardous material without touching—AEM mapping of Norwegian alum shale. *First Break* **2017**, *35*, 89807. [[CrossRef](#)]
- Auken, E.; Boesen, T.; Christiansen, A.V. A review of airborne electromagnetic methods with focus on geotechnical and hydrological applications from 2007 to 2017. *Adv. Geophys.* **2017**, *58*, 47–93. doi: 10.1016/bs.agph.2017.10.002. [[CrossRef](#)]
- Engebretsen, K.W.; Zhang, B.; Fiandaca, G.; Madsen, L.M.; Auken, E.; Christiansen, A.V. Accelerated 2.5-D inversion of airborne transient electromagnetic data using reduced 3-D meshing. *Geophys. J. Int.* **2022**, *230*, 643–653. [[CrossRef](#)]
- Heagy, L.J.; Cockett, R.; Kang, S.; Rosenkjaer, G.K.; Oldenburg, D.W. A framework for simulation and inversion in electromagnetics. *Comput. Geosci.* **2017**, *107*, 1–19. doi: 10.1016/j.cageo.2017.06.018. [[CrossRef](#)]
- Cai, H.; Hu, X.; Xiong, B.; Auken, E.; Han, M.; Li, J. Finite element time domain modeling of controlled-source electromagnetic data with a hybrid boundary condition. *J. Appl. Geophys.* **2017**, *145*, 133–143. [[CrossRef](#)]
- Yin, C.; Qi, Y.; Liu, Y. 3D time-domain airborne EM modeling for an arbitrarily anisotropic earth. *J. Appl. Geophys.* **2016**, *131*, 163–178. [[CrossRef](#)]
- Ansari, S.; Farquharson, C.; MacLachlan, S. A gauged finite-element potential formulation for accurate inductive and galvanic modelling of 3-D electromagnetic problems. *Geophys. J. Int.* **2017**, *210*, 105–129. [[CrossRef](#)]
- Börner, R.U.; Ernst, O.G.; Güttel, S. Three-dimensional transient electromagnetic modelling using rational Krylov methods. *Geophys. J. Int.* **2015**, *202*, 2025–2043. [[CrossRef](#)]
- Cox, L.H.; Wilson, G.A.; Zhdanov, M.S. 3D inversion of airborne electromagnetic data using a moving footprint. *Explor. Geophys.* **2010**, *41*, 250–259. [[CrossRef](#)]
- Oldenburg, D.W.; Li, Y. Estimating depth of investigation in dc resistivity and IP surveys. *Geophysics* **1999**, *64*, 403–416. [[CrossRef](#)]
- Binley, A.; Kemna, A. DC resistivity and induced polarization methods. In *Hydrogeophysics*; Springer: Berlin/Heidelberg, Germany, 2005; pp. 129–156.
- Caterina, D.; Beaujean, J.; Robert, T.; Nguyen, F. A comparison study of different image appraisal tools for electrical resistivity tomography. *Surf. Geophys.* **2013**, *11*, 639–658. [[CrossRef](#)]
- Paepen, M.; Deleersnyder, W.; De Latte, S.; Walraevens, K.; Hermans, T. Effect of Groundwater Extraction and Artificial Recharge on the Geophysical Footprints of Fresh Submarine Groundwater Discharge in the Western Belgian Coastal Area. *Water* **2022**, *14*, 1040. [[CrossRef](#)]
- Alumbaugh, D.L.; Newman, G.A. Image appraisal for 2-D and 3-D electromagnetic inversion. *Geophysics* **2000**, *65*, 1455–1467. [[CrossRef](#)]
- Christiansen, A.V.; Christensen, N.B. A quantitative appraisal of airborne and ground-based transient electromagnetic (TEM) measurements in Denmark. *Geophysics* **2003**, *68*, 523–534. [[CrossRef](#)]
- Werthmüller, D. An open-source full 3D electromagnetic modeler for 1D VTI media in Python: Empymod. *Geophysics* **2017**, *82*, WB9–WB19. doi: 10.1190/geo2016-0626.1. [[CrossRef](#)]
- Hunziker, J.; Thorbecke, J.; Slob, E. The electromagnetic response in a layered vertical transverse isotropic medium: A new look at an old problem. *Geophysics* **2015**, *80*, F1–F18. [[CrossRef](#)]
- Constable, S.C.; Parker, R.L.; Constable, C.G. Occam’s inversion: A practical algorithm for generating smooth models from electromagnetic sounding data. *Geophysics* **1987**, *52*, 289–300. [[CrossRef](#)]
- Tikhonov, A.N. On the stability of inverse problems. *Proc. Dokl. Akad. Nauk SSSR* **1943**, *39*, 195–198.
- Zhang, B.; Engebretsen, K.W.; Fiandaca, G.; Cai, H.; Auken, E. 3D inversion of time-domain electromagnetic data using finite elements and a triple mesh formulation. *Geophysics* **2021**, *86*, E257–E267. [[CrossRef](#)]
- Delsman, J.; van Baaren, E.; Vermaas, T.; Karaoulis, M.; Bootsma, H.; de Louw, P.; Pauw, P.; Oude Essink, G.; Dabekaussen, W.; Van Camp, M.; et al. *TOPSOIL Airborne EM Kartering Van Zoet en Zout Grondwater in Vlaanderen*; Technical Report; VMM: Aalst, Belgium, 2019.
- Sørensen, K.; Auken, E. SkyTEM? A new high-resolution helicopter transient electromagnetic system. *Explor. Geophys.* **2004**, *35*, 194–202. [[CrossRef](#)]

29. Hansen, P.C. *Discrete Inverse Problems: Insight and Algorithms*; Society for Industrial and Applied Mathematics: Philadelphia, PA, USA, 2010; Volume 7.
30. Flanders Environment Agency; Vandeveld, D.; Lermytte, J. Airborne EM data (Belgium) from flight line 306025. *Zenodo* **2022**. Available online: <https://doi.org/10.5281/zenodo.7015419> (accessed on 1 May 2022).
31. Deleersnyder, W. WouterDls/AEM_Appraisal: First Release (0.0.0). *Zenodo* **2022**. Available online: <https://doi.org/10.5281/zenodo.7015876> (accessed on 1 May 2022).
32. Cockett, R.; Kang, S.; Heagy, L.J.; Pidlisecky, A.; Oldenburg, D.W. SimPEG: An open source framework for simulation and gradient based parameter estimation in geophysical applications. *Comput. Geosci.* **2015**, *85*, 142–154. doi: 10.1016/j.cageo.2015.09.015. [[CrossRef](#)]
33. Ward, S.H.; Hohmann, G.W. *Electromagnetic Theory for Geophysical Applications Version 4*; Society of Exploration Geophysicists: Houston, TX, USA, 1988.
34. Deleersnyder, W.; Hermans, T.; Dudal, D. An efficient Gaussian process regression surrogate model for Airborne TDEM multidimensional modelling. 2022, *manuscript in preparation*.